

# **Mid-Infrared Emission Features in the ISM:**

## **Feature-to-Feature Flux Ratios**

Nanyao Y. Lu

Infrared Processing and Analysis Center

MS 100-22, Caltech

Pasadena, CA 91125

Email: lu@ipac.caltech.edu

Received \_\_\_\_\_; accepted \_\_\_\_\_

*Submitted to ApJ Letters*

## ABSTRACT

Using a limited, but representative sample of sources in the ISM of our Galaxy with published spectra from the *Infrared Space Observatory*, we analyze flux ratios between the major mid-IR emission features (EFs) centered around 6.2, 7.7, 8.6 and 11.3  $\mu\text{m}$ , respectively. In a flux ratio-to-flux ratio plot of  $\text{EF}(6.2\,\mu\text{m})/\text{EF}(7.7\,\mu\text{m})$  as a function of  $\text{EF}(11.3\,\mu\text{m})/\text{EF}(7.7\,\mu\text{m})$ , the sample sources form roughly a  $\Lambda$ -shaped locus which appear to trace, on an overall basis, the hardness of a local heating radiation field. But some driving parameters other than the radiation field may also be required for a full interpretation of this trend. On the other hand, the flux ratio of  $\text{EF}(8.6\,\mu\text{m})/\text{EF}(7.7\,\mu\text{m})$  shows little variation over the sample sources, except for two HII regions which have much higher values for this ratio due to an “ $\text{EF}(8.7\,\mu\text{m})$  anomaly,” a phenomenon clearly associated with environments of an intense far-UV radiation field. If further confirmed on a larger database, these trends should provide crucial information on how the EF carriers collectively respond to a changing environment.

*Subject headings:* Infrared: lines and bands – ISM: general

## 1. Introduction

Since they were first discovered about two decades ago (Gillett et al. 1973), the mid-IR emission features (EFs), i.e., those broad emission bands centered respectively at 6.2, 7.7, 8.6 and 11.3  $\mu\text{m}$ , have been detected from a variety of sources in our own Galaxy as well as in some other galaxies. This makes it rather clear that the carriers of these EFs play a significant role in regulating the physical conditions in the ISM. One concept that has gained popularity is that these EFs arise from the vibrational modes of the so-called aromatic hydrocarbon molecules (hereafter PAHs; Léger & Puget 1984; Allamandola et al. 1985). However, this is largely based on a wavelength coincidence between the observed EFs and the absorption bands measured in laboratories, a criterion that other candidate EF carriers (e.g., Papoular et al. 1989; Sakata et al. 1984) also seem to satisfy. It is therefore important to test this PAH and other candidate scenarios in as many ways as possible. One possible way is to observe how the strength ratios between the EFs react to a changing heating radiation field in the ISM. This approach is viable because, for example, if EFs arise from PAHs, some of their feature-to-feature strength ratios should depend on the hardness of the heating radiation field via factors such as the fraction of PAH cations (i.e., singly ionized PAHs; Langhoff 1996) and the degree of dehydrogenation (e.g., Jourdain de Muizon et al. 1990). Because of the limited sensitivity and spectral coverage associated with sub-orbital platform observations, studies on how features respond to a changing environment have been carried out so far only to a limited extent (e.g., Cohen et al. 1986; Joblin et al. 1996).

With its unprecedented sensitivity and continuous spectral coverage, the Infrared Space Observatory (ISO; Kessler et al. 1996) has been used to obtain mid-IR spectra of sources in a variety of environments ranging over far-UV intense to typical diffuse ISM. This makes it possible for the first time to study the relative strengths among all the

major EFs under a wide range of physical conditions. We gather here the published ISO mid-IR spectra on a limited, but representative set of sources in the ISM of our Galaxy to seek possible correlations between the feature-to-feature flux ratios and the local heating radiation field. While the former parameters are measured directly from the ISO spectra, the latter is inferred from the properties of the stars that likely dominate the radiation field at the locations where the ISO spectra were taken.

In Sect. 2 we describe the sample, the data and how we evaluate the integrated flux of a feature. In Sect. 3 we analyze feature-to-feature flux ratios and identify some possible systematic trends. Some implications from these trends are discussed in Sect. 4, when applicable, in comparison with the current knowledge of PAHs.

## 2. The Data

Our sample sources are listed in column (1) of Table 1, grouped into the following categories based on how hard their local radiation fields are likely to be: (1) the five compact HII regions with the highest S/N ratios in Roelfsema et al. (1996) and the HII region in the M17 complex from Verstraete et al. (1996); (2) two photodissociation regions (PDRs) in the M17 region also from Verstraete et al. (1996); (3) three reflection nebulae: a cloud edge in Ophiuchus from Boulanger et al. (1996), NGC 7023 from Cesarsky et al. (1996a), and vdB 133 from Uchida et al. (1998); and (4) the two brightest spectra taken along the Galactic plane in Mattila et al. (1996). To supplement this last category of the weakest sources in the sample, we also included two published spectra along the inner Galactic plane taken with IRTS from Onaka et al. (1996) and an ISO spectrum from Boulade (1996) of the interstellar medium in the central part of NGC 5195, a galaxy with very few stars younger than B5. The corresponding instrument is given in column (2) in the table, where SWS stands for the ISO short-wavelength spectrometer (de Graauw et al. 1996),

CAM-CVF refers to the ISO-CAM with its circular variable filters (Cesarsky et al. 1996b), and PHT-S refers to the spectroscopic mode of ISOPHOT (Lemke et al. 1996). Most of these ISO spectra were published as part of the first ISO results. While their absolute flux scale and sky subtraction may need further improvement, the quoted relative accuracy over the wavelength range of 6 to  $12\mu\text{m}$  is better than 20%. To avoid the problem of spectral resolution inhomogeneity over the sample sources, we consider only the integrated feature fluxes that are drawn directly from the published figures.

We subtract a linear “continuum” (in  $F_\lambda$ ) from each emission feature as follows: For the emission feature at  $6.2\mu\text{m}$  [hereafter EF(6.2), similarly for the other features], this is a line connecting the mean spectral value around  $5.9\mu\text{m}$  to that around  $6.9\mu\text{m}$ ; for EF(7.7) and EF(8.6), a line drawn in a similar way from  $6.9\mu\text{m}$  to  $9.9\mu\text{m}$ ; and for EF(11.3), a line from  $10\mu\text{m}$  to  $12\mu\text{m}$ . Clearly, these continuum definitions are largely subjective and somewhat oversimplified. But a more accurate continuum definition should not change our results in a significant way. Also, for the PHT-S and IRTS spectra which extend only up to about  $11.6\mu\text{m}$  in wavelength, we determine only lower and upper limits on the continuum for EF(11.3) as described in the next paragraph.

After the continuum subtraction, the spectrum of each EF is binned into a histogram with a bin size of  $\sim 0.1\mu\text{m}$  in order to evaluate its integrated flux. The integration is done as follows: the flux of EF(6.2) is an integration of the spectrum from  $6.0$  to  $6.6\mu\text{m}$  in wavelength; for EF(7.7), from  $7.2$  to  $8.1\mu\text{m}$ ; for EF(8.6), from  $8.1$  to  $9.9\mu\text{m}$ ; and for EF(11.6), from  $10.5$  to  $12\mu\text{m}$ . For the PHT-S and IRTS data, we determine only an upper limit and a lower limit on the flux of EF(11.3) as follows: The upper limit is measured from the spectrum after subtracting out a continuum with a fixed  $F_\lambda$  equal to that around  $10\mu\text{m}$ . In this case, the part of EF(11.3) that is beyond the wavelength cutoff of the spectrometer is accounted for by assuming a symmetric profile with respect to the wavelength of the

feature peak. For the PHT-S data, the lower flux limit is obtained by integrating the spectrum up to  $11.6\,\mu\text{m}$  after subtracting out a linear continuum in  $F_\lambda$  connecting the mean spectral value around  $10\,\mu\text{m}$  to that at  $11.6\,\mu\text{m}$ . For the low-resolution IRTS data that appear to lose a large fraction of EF(11.3), we take a loose lower flux limit that equals 60% of the upper limit. The procedure used here should introduce an uncertainty of  $\lesssim 20\%$  in the integrated flux. Also, any systematic effect of this uncertainty on the feature-to-feature ratios should be more or less uniform over the whole sample.

Our results are given in columns (3) to (5) in Table 1 in terms of the following feature-to-feature flux ratios: EF(6.2)/EF(7.7), EF(8.6)/EF(7.7) and EF(11.3)/EF(7.7), where and hereafter in this letter we simply use, for example, EF(6.2)/EF(7.7) to refer to the flux ratio of EF(6.2) to EF(7.7). EF(7.7) is chosen to be the common denominator for minimizing, on an overall basis, the wavelength baselines used in these ratios. Also listed in Table 1 are the known or estimated spectral types of the dominant heating stars in column (6) and estimated mean dust temperatures in column (7). For each of the compact HII regions, this spectral type was derived, under a single-star heating assumption, by comparing the models of zero-age main sequence stars in Panadia (1973) with a Lyman-continuum luminosity inferred from the total IR luminosity of the HII region given in Table 1 of Roelfsema et al. (1996). The slope of this linear Lyman-continuum/IR relation was determined using the measured number of the Lyman-continuum photons in the case of IRAS 18116-1646 (Garay et al. 1993). The dust temperature is derived from a  $\lambda^{-1}$  emissivity and the following far-infrared continuum fluxes: for the compact HII regions and NGC 5195, we used the 60 and  $100\,\mu\text{m}$  flux densities in the IRAS Point Source Catalog; for the 3 regions in M17, we used the 50 and  $100\,\mu\text{m}$  maps in Gatley et al. (1976); for NGC 7023, we used the far-IR maps in Whitcomb et al. (1981); for Ophiuchus and the spectra along the Galactic plane, we measured their 60 and  $100\,\mu\text{m}$  surface brightness values on the IRAS Sky Survey Atlas plates; and for vdB 133, the IRAS surface brightness

values in Sellgren (1990) were used here. We emphasize that both the spectral types and dust temperatures given in Table 1 are for *indicative* purpose in this paper. In some cases, there is some uncertainty as to whether they represent the actual physical condition within the area where the mid-IR spectrum was observed.

### 3. Feature-to-Feature Flux Ratios

Using these feature-to-feature flux ratios, we construct two pairwise plots in Fig. 1 where different symbols are used to differentiate the various source categories in Table 1: the 6 HII regions are represented by filled squares; the 2 PDRs by open squares; the three reflection nebulae by crosses; the 4 spectra along the Galactic plane by horizontal bars each extending from the lower limit to the upper limit on the value of  $EF(11.3)/EF(7.7)$  as given in Table 1; and the galaxy NGC 5195 by an asterisk. The typical errors are on the order of 30% or less along either axis. There are two HII regions which are further circled in Fig. 1. These are what we define below as sources with an “EF(8.6) anomaly.”

#### 3.1. Relative Strengths between EF(7.7) and EF(8.6)

Fig. 1a is a plot of  $EF(8.6)/EF(7.7)$  as a function of  $EF(11.3)/EF(7.7)$ . Apparently, the sources are distributed into two distinct groups on this plot. One group consists of the compact HII region IRAS 18434-0242 and the HII region in M17. These two sources are characterized by  $EF(8.6)/EF(7.7) \sim 1.5$ , a value which is at least three times as large as that of any source in the other group made of the other sample sources. For the latter group, the ratios of  $EF(8.6)/EF(7.7)$  do not change significantly, with a group mean of 0.40 and a standard deviation of only 0.07. Since the majority of the sources (both Galactic and extragalactic) with published mid-IR spectra so far belong more or less to the latter group,

we refer to the phenomenon that  $\text{EF}(8.6)/\text{EF}(7.7) > 1$  as an “EF(8.6) anomaly” in this letter.

Both of the EF(8.6)-anomaly sources have a mid-IR continuum that rises steeply toward longer wavelengths, about 3 to 5 times steeper than the continuum of any of the other HII regions in the sample (see Roelfsema et al. 1996; Verstraete et al. 1996) or 2 to 3 times steeper than that of the hottest knot in the Antennae galaxies (Vigroux et al. 1996) when the spectral steepness is measured in terms of the ratio of the flux density at  $12\mu\text{m}$  to that at  $6\mu\text{m}$ . This strongly suggests a presence, within the SWS aperture, of a very hot continuum from dust grains heated by an intense far-UV radiation field in these EF(8.6)-anomaly sources. A closer look at the spectra of the EF(8.6)-anomaly sources shows that EF(8.6) is not only stronger than EF(7.7) in peak intensity but also extends to a much wider wavelength range than that in any “EF(8.6)-normal” source.

### 3.2. Relative Strengths among EF(6.2), EF(7.7) and EF(11.3)

In Fig. 1b, a plot of  $\text{EF}(6.2)/\text{EF}(7.7)$  as a function of  $\text{EF}(11.3)/\text{EF}(7.7)$ , the data points apparently form a locus that roughly resembles a  $\Lambda$ -shaped curve centered at  $\text{EF}(11.3)/\text{EF}(7.7) \sim 0.3$ . What may be significant is that the various source categories seem to occupy different segments of the curve: all the HII regions but one (IRAS 22308+5812) lie near the end of the curve characterized by small values for both  $\text{EF}(6.2)/\text{EF}(7.7)$  and  $\text{EF}(11.3)/\text{EF}(7.7)$ ; the 2 PDRs are on the same side of the curve as the HII regions, but located somewhat closer to the top of the curve where the three reflection nebulae are located; and on the other side of the curve are the spectra taken along the inner Galactic plane and that of NGC 5195, presumably dominated by the emission from the diffuse ISM.

If the sources in the diffuse ISM category are indeed excited mainly by somewhat late



type stars, our data suggests that there exists a well defined area in Fig. 1b for sources heated by a radiation field of a certain range of hardness. The only clear exception to this interpretation is IRAS 22308+5812, the HII region that is in close proximity to the three reflection nebulae in Fig. 1b. This source actually has a mid-IR spectrum with little indication of a hot dust continuum rising toward longer wavelengths. This is more like the spectra of reflection nebulae than those of the other HII regions in the sample. In this sense, its location in Fig. 1b may not be very surprising.

On the other hand, if the dust temperature given in column (7) of Table 1 reflects the mean intensity of a radiation field, it seems quite clear that the radiation intensity can not be the primary driving force on how a source will be located in Fig. 1b. For example, the overall radiation intensity in NGC 5195 is comparable to those in some of the compact HII regions and is certainly stronger than that in the Ophiuchus nebula. But NGC 5195 is clearly located closer to the other diffuse sources in Fig. 1b. Another example comes from NGC 7023 and the Ophiuchus nebula, which lie close to each other in Fig. 1b. These two sources have a similar stellar energy distribution, but are exposed to a very different radiation intensity.

It should also be pointed out that, although the trend with the radiation field in Fig. 1b seems to be quite significant from one source category to another, it is still unclear how good it is within each source category. For example, it is reasonable to assume that the two EF(8.6)-anomaly sources represent the hardest UV fields in the sample, but they are not at the extreme end of the trend in Fig. 1b. Another example is vdB 133, a reflection nebula that may be excited mainly by a star of spectral type F5 (Uchida et al. 1998). However, in terms of EFs, vdB 133 is quite similar to the other two nebulae excited by much hotter stars. As a result of the small numbers of sources involved and the still large measurement errors, the certainty about these details of the trend in Fig. 1b is not as high as that about

its overall pattern. But it seems fair to say that although the heating radiation field plays a crucial role in determining the relative strengths of EFs, but there may be other regulators as well.

#### 4. Discussion

The result of Fig. 1a that the ratios of  $\text{EF}(8.6)/\text{EF}(7.7)$  for EF(8.6)-normal sources stay nearly constant is already quite secure at this point. This suggests either (a) that there is roughly a fixed ratio between the strengths of these two EFs or (b) that EF(7.7) has a long wavelength tail/plateau that dominates the integrated flux of EF(8.6) as a result of our dividing the two EFs at  $8.1\ \mu\text{m}$  in evaluating their fluxes. Under the current framework of PAHs, however, the ratio for  $\text{EF}(8.6)/\text{EF}(7.7)$  is expected to decrease with an increasing degree of dehydrogenation associated with an increasing hardness of the heating radiation field (Jourdain de Muizon et al. 1990). So the laboratory results on PAHs favor (b).

On the other hand, additional and improved data are probably needed for further confirmation on the details of the distribution pattern in Fig. 1b. There is a slight possibility that, once more data points are inserted in Fig. 1b, a simpler pattern [e.g.,  $\text{EF}(6.2)/\text{EF}(7.7)$  increases somewhat as  $\text{EF}(11.3)/\text{EF}(7.7)$  decreases] could emerge. However, if this  $\Lambda$ -shaped distribution pattern is further confirmed, it could provide new constraints on the identification of the EF carriers. For example, the right side of the  $\Lambda$ -shaped curve in Fig. 1b may be consistent with a picture where one has a combination of rising PAH temperature and increasing ionization effect (Langhoff et al. 1996) as one goes up along the curve. However, the current knowledge of PAHs does not seem to suggest a turnaround in  $\text{EF}(6.2)/\text{EF}(7.7)$ . An increasing photodestruction effect does suggest a decreasing ratio of  $\text{EF}(6.2)/\text{EF}(7.7)$  as smaller PAHs are easier to be destroyed than their larger cousins (Allamandola et al. 1989; Allain, Leach, & Sedlmayr 1996a, 1996b) and as larger PAHs

reach lower peak temperatures after absorbing a UV photon (Léger & Puget 1989). But the wavelength difference between the two features is so small that the dependence of their ratio on the PAH size distribution seems inadequate to explain the observed large change in  $EF(6.2)/EF(7.7)$ . Besides, this effect has to be counter-balanced by the fact that in an increasingly harder UV-rich environment, the average PAH temperature also gets hotter. Perhaps, this implies that something in addition to the radiation field is needed to explain the distribution pattern in Fig. 1b.

The laboratory counterpart of the  $EF(8.6)$ -anomaly phenomenon is unknown at this point. One speculation is that both  $EF(7.7)$  and  $EF(8.6)$  are stronger relative to the other features in a far-UV rich environment. Perhaps, the two features sit on top of an emission plateau whose contribution to the fluxes of  $EF(7.7)$  and  $EF(8.6)$  becomes relatively important only under an intense far-UV radiation field. In fact, such an emission plateau may put the  $EF(8.6)$ -anomaly phenomenon in a sequence between those  $EF(8.6)$ -normal sources and those with even more “unusual”  $EF$  spectra, e.g., an ISO spectrum dominated by a previously unknown broad feature around  $8\mu\text{m}$  seen in an ultra compact HII region (Cesarsky et al. 1996c) to those featureless spectra seen in many active galactic nuclei (e.g., Aitken & Roche 1985).

Regardless of how consistent they are with the physical properties of a specific class of candidates for the  $EF$  carriers, the trends in Fig. 1 should inevitably lead us to a more complete picture on how the relative  $EF$  strengths change from one type of environment to another. A direct application of this would be to help interpreting the global  $EF$  spectra from galaxies. For example, a preliminary analysis shows that in a plot such as Fig. 1b, most normal galaxies scatter within a region close to that occupied by those data points taken along the inner Galactic plane (Lu et al. 1998), suggesting that the global  $EF$ s of a galaxy may be dominated by the emission from the diffuse ISM component.

The author is grateful to the anonymous referee for a number of comments and suggestions that helped improving both the presentation and interpretation of the data, to L. Allamandola and D. Hudgins for interesting conversations on PAHs, and to G. Helou, S. Malhotra and C. Xu for helpful comments. This work was supported in part by Jet Propulsion Laboratory, California Institute of Technology, under a contract with the National Aeronautics and Space Administration.

## REFERENCES

- Aitken, D. A., & Roche, P. F. 1985, MNRAS, 213, 777
- Allain, T., Leach, S., & Sedlmayr, E. 1996a, A&A, 305, 602
- Allain, T., Leach, S., & Sedlmayr, E. 1996b, A&A, 305, 616
- Allamandola, L. J., Tielens, A. G. G. M., & Barker, J. R. 1985, ApJ, 290, L25
- Allamandola, L. J., Tielens, A. G. G. M., & Barker, J. R. 1989, ApJS, 71, 733
- Boulade, O., et al. 1996, A&A, 315, L85
- Boulanger, F., et al. 1996, A&A, 315, L325
- Cesarsky, D., Lequeux, J., Abergel, A., Perault, M., Palazzi, E., Madden, S., Tran, D.  
1996a, A&A, 315, L305
- Cesarsky, C. et al. 1996b, A&A, 315, L32
- Cesarsky, D., Lequeux, J., Abergel, A., Perault, M., Palazzi, E., Madden, S., & Tran, D.  
1996c, A&A, 315, L309
- Cohen, M., Allamandola, L. J., Tielens, A. G. G. M., Bregman, J., Simpson, J. P.,  
Wittebore, F. C., Wooden, D., & Rank, D. 1986, ApJ, 302, 737
- de Graauw, T., et al. 1996, A&A, 315, L49
- Garay, G., Rodríguez, L. F., Moran, J. M., & Churchwell, E. 1993, ApJ, 418, 368
- Gatley, I., Becklin, E. E., Sellgren, K., Werner, M. W. 1979, ApJ, 233, 575
- Gillett, F. C., Forrest, W. J., & Merrill, K. M. 1973, ApJ, 183, 87
- Joblin, C., Tielens, A. G. G. M., Geballe, T. R., & Wooden, D. H. 1996, ApJ, 460, L119
- Jourdain de Muizon, M., d'Hendecourt, L. B., & Geballe, T. R. 1990, A&A, 227, 526
- Kessler, M. F., et al. 1996, A&A, 315, L27

- Langhoff, S. R. 1996, *J. Phys. Chem.*, 100, 2819
- Léger, A., & Puget, J. L. 1984, *A&A*, 137, L5
- Lemke, D., et al. 1997, *A&A*, 315, L64
- Lu, N. Y., et al. 1998 (in preparation)
- Mattila, K., Lemke, D., Haikala, L. K., Laureijs, R. J., Léger, A., Lehtinen, K., Leinert, Ch., & Mezger, P. G. 1996, *A&A*, 315, L353
- Onaka, T., Yamamura, I., Tanabé, T., Roellig, T. L., & Yuen, L. 1996, *PASJ*, 48, L59
- Panagia, N. 1973, *AJ*, 78, 929
- Papoular, R., Conard, J., Giuliano, M., Kister, J., & Mille, G. 1989, *A&A*, 217, 204
- Puget, J. L., & Léger, A. 1989, *ARA&A*, 27, 161
- Roelfsema, P. R., et al. 1996, *A&A*, 315, L289
- Sakata, A., Wada, S., Tanabé, T., Onaka, T. 1984, *ApJ*, 287, L51
- Sellgren, K., Luan, L., & Werner, M. W. 1990, *ApJ*, 359, 384
- Uchida, K. I., Sellgren, K., & Werner, M. 1998, *ApJ*, 493, L109
- Verstraete, L., Puget, J. L., Falgarone, E., Drapatz, S., Wright, C. M., & Timmermann, R. 1996, *A&A*, 315, L337
- Vigroux, L., et al. 1996, *A&A*, 315, L93
- Whitcomb, S. E., Gatley, I., Hildebrand, R. H., Keene, J., Sellgren, K., Werner, M. W. 1981, *ApJ*, 246, 416

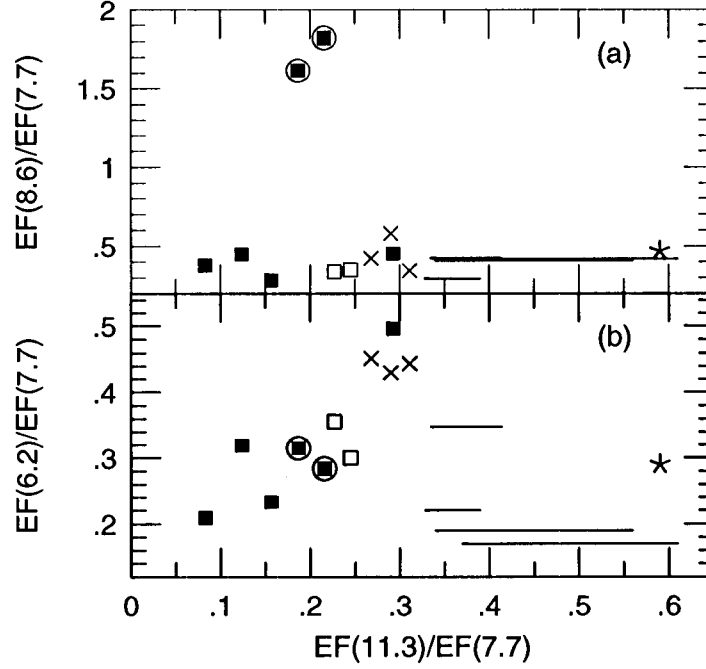


Fig. 1.— Plots of feature-to-feature flux ratios for the sources listed in Table 1: (a)  $EF(8.6)/EF(7.7)$  vs.  $EF(11.3)/EF(7.7)$  and (b)  $EF(6.2)/EF(7.7)$  vs.  $EF(11.3)/EF(7.7)$ . We use filled squares to represent the 6 HII regions, with the two HII regions of the largest  $EF(8.7)/EF(7.7)$  ratios further circled; open squares for the two PDR regions; crosses for the three reflection nebulae; horizontal bars for the diffuse ISM emissions along the Galactic plane, each extending between the lower and upper limits on the value of  $EF(11.3)/EF(7.7)$  as given in Table 1; and an asterisk for the galaxy NGC 5195. The typical errors are on the order of 30% or less along either axis.

Table 1. Flux Ratios of Mid-IR Emission Features

Source	Instrument	(6.2)/(7.7)	(8.6)/(7.7)	(11.3)/(7.7)	Spec. Type	$T_{dust}$
(1)	(2)	(3)	(4)	(5)	(6)	(7)
<b>HII regions:</b>						
IRAS 18434-0242 <sup>a</sup>	SWS	0.32	1.62	0.19	O6	38
IRAS 18116-1646 <sup>a</sup>	SWS	0.32	0.45	0.12	O6.5	36
IRAS 22308+5812 <sup>a</sup>	SWS	0.50	0.45	0.29	O7	38
IRAS 19442+2427 <sup>a</sup>	SWS	0.21	0.38	0.08	O8	38
IRAS 18162-2048 <sup>a</sup>	SWS	0.23	0.28	0.16	O9	40
M17 HII <sup>b</sup>	SWS	0.28	1.82	0.22	O	58
<b>PDRs:</b>						
M17 Interface <sup>b</sup>	SWS	0.36	0.34	0.23	O	48
M17 H <sub>2</sub> -cloud <sup>b</sup>	SWS	0.30	0.35	0.24	O	39
<b>Reflect. Nebulae:</b>						
Ophiuchus <sup>c</sup>	CAM-CVF	0.44	0.34	0.31	B2	30
NGC 7023 North <sup>d</sup>	CAM-CVF	0.45	0.42	0.27	B3	50
vdB 133 <sup>e</sup>	CAM-CVF	0.43	0.58	0.29	F5/B7	30
<b>Diffuse ISM:</b>						
( $l = 355^\circ, b = 0^\circ$ ) <sup>f</sup>	PHT-S	0.35	0.42	0.34–0.41	...	27
( $l = 330^\circ, b = 0^\circ$ ) <sup>f</sup>	PHT-S	0.22	0.29	0.33–0.39	...	27
( $l \approx 44.3^\circ, b \approx -20'$ ) <sup>g</sup>	IRTS	0.17	0.42	0.37–0.61	...	26
( $l \approx 51.5^\circ, b \approx 1.5^\circ$ ) <sup>g</sup>	IRTS	0.19	0.41	0.34–0.56	...	25
NGC 5195 <sup>h</sup>	CAM-CVF	0.29	0.47	0.59	...	35

References: (a) Roelfsema et al. (1996); (b) Verstraete et al. (1996); (c) Boulanger et al. (1996);  
(d) Cesarsky et al. (1996a); (e) Uchida et al. (1998); (f) Mattila et al. (1996);  
(g) Onaka et al. (1996); and (h) Boulade et al. (1996).